Applied Ocean Research 166 (2026) 104921

Contents lists available at ScienceDirect

Applied Ocean Research

journal homepage: www.elsevier.com/locate/apor

Research paper

Model validation and improved PTO modeling of a field-deployed wave energy converter with tethered heave plate

David Okushemiya [a,b,*], Curtis J. Rusch [c], Bryson Robertson [a,b], Zhe Zhang [d]

[a] Pacific Marine Energy Center, Oregon State University, Corvallis, 97333, OR, USA
[b] Civil and Construction Engineering, Oregon State University, Corvallis, 97333, OR, USA
[c] Applied Physics Laboratory, University of Washington, 1013 NE 40th St, Seattle, 98105, WA, USA
[d] Columbia Power Technologies, Inc, 4920 SW 3rd St Ste A, Corvallis 97333, OR, USA

ARTICLE INFO

Keywords:
Wave energy
Numerical modeling
Model validation
Field testing
WEC with tethered heave plate
Dynamometer testing
Underwater vehicle charging

ABSTRACT

Rigorous incremental testing and validation are essential to advancing wave energy converter (WEC) technology. Although laboratory wave tank testing remains common, it poses challenges in scaling hydrodynamic responses and power take-off (PTO) dynamics. These issues are more pronounced for WECs with tethered heave plates due to complex interactions between the structure, tether, heave plate, and PTO; all of which often exceed tank depth and scaling limits. Field testing enables full-system evaluation but introduces practical limitations, including environmental variability, limited sensing, and measurement uncertainty. A knowledge gap remains in how to overcome these limitations to extract meaningful insights and validate WEC numerical models using field test data. Moreover, full-scale PTOs exhibit significant nonlinearities, such as generator inertia, internal losses, and inefficiencies across the full energy conversion chain, that are not captured in current PTO models. This highlights the need for improved modeling techniques to realistically estimate useful power and energy output. This study uses a field-deployed WEC with a tethered heave plate to demonstrate how combining statistical and spectral analyses enables comprehensive insight and validation of WEC models using field data. It also advances PTO modeling by incorporating generator inertia and fitting a parametric relationship between shaft speed and useful power based on PTO dynamometer test data. This approach predicted power and energy within 9% of field measurements, whereas conventional models overestimated these output by up to a factor of 3. The improved PTO modeling yields more realistic levelized cost of energy (LCOE) estimates to better guide future full-scale WEC development.

1. Introduction

There continues to be increasing opportunity for wave energy as a source of renewable energy for both utility and smaller scale power applications. Wave energy has the potential to make a significant contribution to both global energy needs, and also as a source of renewable power for smaller loads, such as autonomous underwater vehicles (AUV). However, the design and modeling of Wave Energy Converters (WECs) is a complex and challenging task, resulting in high uncertainties in evaluating performance, cost, and overall economic viability of WECs (Czech and Bauer, 2012). Understanding and addressing these uncertainties requires rigorous testing and validation at multiple stages of a WEC development. (Guo and Ringwood, 2021; Jin and Greaves).

Traditionally, scaled laboratory wave tank testing of WECs has been the most useful method of testing and validation (Pecher, 2017). However, as WEC designs evolve and become more complex, this method presents numerous shortfalls, including accurately scaling all hydrodynamic phenomena, material properties, depth limitations, and Power Take Off (PTO) electro-mechanical dynamics (Ruzzo et al., 2021; Sheng et al., 2014). This limits the suitability of scaled tank testing and necessitates greater reliance on real-world field testing. While field testing allows full-scale testing and validation, it introduces practical limitations such as uncontrolled environmental conditions, limited sensing, and difficulty in capturing precise wave elevation at the exact WEC location, making it difficult to gain direct insights from numerical validation. With the growing availability of permitted field test sites (e.g., EMEC (Norris and Droniou, 2007), PacWave (Freeman et al., 2022), WETS (Li and Cheung, 2014), Albany Australia (Gaudin et al., 2018)), there is a significant need to develop and demonstrate a comprehensive method for extracting insights and validating WEC models using field data. Furthermore, full scale PTOs in field testing

* Corresponding author at: Civil and Construction Engineering, Oregon State University, Corvallis, 97333, OR, USA.
E-mail address: okushemd@oregonstate.edu (D. Okushemiya).

https://doi.org/10.1016/j.apor.2026.104921
Received 4 January 2025; Received in revised form 13 October 2025; Accepted 2 January 2026
Available online 6 January 2026

exhibit real nonlinearities, including inertia effects, losses and inefficiencies (Pedersen et al., 2016). They also enable direct measurement of the full energy conversion chain, including the mechanical power at the PTO shaft and resulting useful electrical output from the PTO generator, quantities not captured in tank tests or current numerical models.

These field-scale experimental challenges in WEC development raise two key research questions explored in this study. Firstly, how can the stated practical limitations of field testing be overcome to enable meaningful insights and validation of WEC numerical models, and, secondly, how can generator inertia and PTO internal losses across the full PTO energy conversion chain be incorporated into numerical models, and what impact do they have on evaluating full-scale WEC power performance?

2. Background

Experimental testing remains fundamental in the development and validation of WECs, with the vast majority of published studies relying on scaled laboratory wave tank experiments. Numerous researchers have employed laboratory wave tanks to investigate hydrodynamic response, system behavior, and validate numerical models across various WEC configurations (e.g., Xu et al., 2021; Jin et al., 2023; Beatty et al., 2015; Paduano et al., 2020; Cheng et al., 2022b,a; Xu et al., 2019; Dessi et al., 2022; Yu et al., 2024; Sugiura et al., 2020). In these studies, the full scale WECs were reduced to scaled models by applying well-known scaling laws, such as Froude and Reynolds scaling (Heller, 2011), to scale the dimensions of the structure, the waves, and other forces acting on the device to fit the wave tank capacity (Windt et al., 2021). Although the applied scaling laws are well established, errors and undesired scaling effects are inherent (Windt et al., 2021; Palm et al., 2018). The scaling effects have been found to be closely related to the viscous contribution and the incompatibility between the Reynolds scaling and Froude scaling within physical wave tanks (Windt et al., 2021; Palm et al., 2018). Additionally, Windt et al. (2021) highlights real mechanical effects, such as friction, and generator inertia, as additional scaling limitations in physical wave tank scaled model test. As WEC technology continues to evolve, new archetypes have emerged that further complicate scaled experimental testing. One of such design is the multi-body WEC with a tethered heave plate, such as the system investigated in this study. Unlike the most studied configurations where the heave plates are rigidly connected to the WEC structure (Beatty et al., 2015; Rao et al., 2021; Sheng, 2025), tethered heave plates are suspended at significant depths using long compliant tethers. These longer tethers introduce compliance that helps absorb shock and dynamic tension loads more effectively (Fitzgerald and Bergdahl, 2008). Additionally, the tether introduces design parameters, such as stiffness, that can be tuned to influence the WEC system's response and control. However, long tether lengths introduce depth scaling requirements that exceed the capabilities of most laboratory wave tanks, making even scaled model testing infeasible in such environments.

In addition to depth limitations, difficulty also arises from fiber rope tethers having a dynamic stiffness different from the static stiffness and dependent on the loads, displacement and cycle period (American Bureau of Shipping, 2021). This further complicates the identification of an ideal model scale between the WEC structure, tether, and heave plate. Scaling methods for such devices to undergo testing in laboratory wave tanks remain unresolved.

Another difficulty in physical laboratory wave tank scale model testing lies in the modeling and scaling of power take-off (PTO) systems. PTO systems do not follow conventional scaling laws such as Froude or Reynolds, making it difficult to accurately replicate the behavior of full-scale PTOs at model scale (Giannini et al., 2020). Although PTO damping and stiffness values are commonly used to approximate PTO effects on WEC dynamics in both physical and numerical models, the power output at small scale is often highly sensitive to uncertainty (Beatty et al., 2017). As a result, scaled testing provides limited insight into full-scale power performance, and complicates accurate evaluation and validation at laboratory scales (Beatty et al., 2017). In representing WEC PTO, the choice of control strategy determines which parameters damping and/or stiffness to be applied (Coe et al., 2017). Reactive control schemes require both damping and stiffness, whereas passive control approach relies solely on damping (Wu et al., 2021). In practice, most WEC operate under passive control due to its simplicity (Hong et al., 2014; Darwish and Aggidis, 2022), where optimal damping values are calculated to maximize energy absorption (Zou et al., 2017; Cheng et al., 2022c). These damping values are implemented as translational damping terms (with units N· s/m) for linear PTO generators (Beatty et al., 2015; Zang et al., 2018), or as rotational damping terms (with units N· m· s/rad) for rotary PTOs generator (Muliawan et al., 2013; Cheng et al., 2024). Using these damping terms, numerical models can predict PTO force and power based on the relative motion velocities of the WEC. However, such models typically do not account for internal losses and inefficiencies present in the full-scale energy conversion chain. As a result, they may overestimate the useful power and energy generation of the PTO, which can lead to overly optimistic projections when computing the levelized cost of energy (LCOE), typically calculated as shown in Ringwood (2025). Data from full-scale PTO dynamometer testing (Bacelli et al., 2019; Rusch et al., 2023) offers an opportunity to improve this by characterizing conversion losses and inefficiencies across the energy chain and fitting parametric relationships between shaft speed and useful power and energy from the PTO. While this presents a promising direction, there is limited published work demonstrating such models. Additionally, full-scale PTOs possess non-negligible acceleration-dependent generator inertia, with effects that vary with generator size and sea state, potentially influencing overall WEC dynamics and power output. Despite this, such inertia effects are rarely captured or included in existing numerical PTO models, representing additional gaps in current PTO modeling approaches.

The above literature review indicates that experimental testing and numerical model validation remain fundamental aspects of WEC development. However, most reported studies focus on laboratory-scale experiments, which face known limitations related to hydrodynamic scaling effects, PTO scaling effects and uncertainties, and restricted applicability for some WEC configurations. Several critical gaps remain in WEC experimentation literature. First, field testing and validation studies are still limited in the literature despite their potential to provide full system insights under realistic environmental conditions. This is particularly important for WEC configurations that cannot be readily tested in laboratory wave tanks due to depth and scale constraints. Second, there is a lack of published work involving WECs with tethered heave plates, which introduce unique hydrodynamic and control complexities. Third, current PTO models used in simulations rarely account for generator inertia, internal PTO losses and associated inefficiencies that are present and measurable in full-scale deployments. These gaps underscore the need for field-based validation experiments, and associated methods and enhanced PTO modeling frameworks that can more accurately reflect actual useful power performance.

In response to these knowledge gaps, the objective of this study is to develop and demonstrate an approach to overcome the established practical limitations of field testing to enable validation of WEC numerical models. In addition, the study aims to provide an improved PTO modeling method that incorporates generator inertia and internal losses across the full energy conversion chain to yield more realistic estimates of the useful power and energy generated by WEC's PTO generator. To achieve this, the study employs TigerRAY (Lesemann, 2020), a novel WEC with a tethered heave plate, designed and tested through a collaboration between University of Washington Applied Physics Laboratory, Oregon State University, and Columbia Power Technologies (C-Power), to investigate the potential of at-sea charging for unmanned underwater

vehicles (UUVs). TigerRAY operates as a tethered (floating third-body) dock configuration for coupled WEC and UUV systems as described in Chen et al. (2024), with the tethered heave plate also serving as a docking station for UUV recharging and data transfer. Through this research, we present a comprehensive approach to overcoming the practical limitations in field testing and validation of WEC models, particularly those arising from uncontrolled environmental conditions, imprecise replication of wave characteristics (e.g., heading, phase, elevation, transformation), and deployment-related uncertainties such as anchor positions and cable lengths. Building on the limited literature of field-based WEC model validation (So et al., 2017; Eriksson et al., 2007; Rusch et al., 2022; Leary et al., 2021), whom rely primarily on statistical and averaged values, a spectral-domain approach that enables direct comparison between measured and simulated dynamic responses is introduced. This enables improved assessment of model fidelity in replicating the real-world dynamic behavior under wave excitation and the evaluation of Energy Capture Spectrum (ECS) - which is a crucial metric for WEC performance (Han et al., 2021). We also demonstrate how spectral analysis can be used to examine inter-component dynamic interactions, identify and isolate discrepancies in the numerical model, and inform improved sensor placement strategies for future field testing campaigns. Finally, we demonstrate how to incorporate generator inertia and use PTO bench-testing data to account for internal losses and inefficiencies in numerical PTO models. Ultimately, these efforts are focused on developing, and demonstrating, improved strategies for realistic estimates of the motion, useful power, and energy produced by the WEC.

3. Case study WEC

3.1. Design and operating principles

The TigerRAY WEC, shown in Fig. 1, is a WEC with three surface floats and a tethered heave plate. It consists of a central nacelle housing the power take-off (PTO) and power electronics, connected on either side to two buoyant floats. The float arms are connected to the drive shafts along the nacelle cylinder's centerline axis, protruding from both ends and linked to internal rotary generators on either side constituting a device with two PTOs. The aft PTO is located on the starboard side, while the fore PTO is on the port side.

TigerRAY is approximately 3 m long, with a nacelle diameter of 0.98 m and float diameter of 0.45 m. The aft float lever arm length, measured from the nacelle cylinder's centerline to the aft cylinder's centerline, is 1.32 m, while the fore float lever arm length, measured from the nacelle cylinder's centerline to the fore cylinder's centerline, is 0.81 m. A heave plate is designed to provide a hydrodynamic reaction force for the nacelle and serve as the docking station for an unmanned underwater vehicle. The heave plate is attached to the nacelle using a "Y" shape tether with branches each 3 m long and a tail of approximately 22 m long.

When the device is excited by waves, the floats rotate about the nacelle, causing the drive shaft to spin and generate electricity through a rotary PTO.

3.2. Field test description

Field testing of TigerRAY was conducted in Lake Washington daily between February 6–8, 2023. TigerRAY was allowed to drift with the waves unrestrained (unmoored) during tests.

An SBG ellipse Inertial Measurement Unit (IMU) was located inside the nacelle and measured displacement at 50 Hz. Pressure sensors were mounted to the underside of the nacelle, and recorded at 100 Hz. Encoders on the drive shafts measured float rotation angles around the nacelle, which corresponds to shaft angle position, at 40 Hz. A load cell between the tether and heave plate recorded tether tension at 100 Hz. An SBG ellipse IMU was also placed on the heave plate and measured its displacement at 50 Hz. Power input and output from the power electronic is measured by current and voltage sensors at a frequency of 200 Hz. All sensors recorded for the duration of the field deployment.

Four Surface Wave Instrument Floats with Tracking (SWIFT) buoys (Thomson, 2012) were attached to TigerRAY, tethered inline to one another, and drifting downwind in a straight line as shown in Fig. 2. The SWIFT buoys operate at a sampling frequency of 25 Hz. Detailed information on the theoretical principles, capabilities, and specifications of the SWIFT buoys is available in Thomson (2012).

The waves measured were wind-driven due to the fetch limited nature of Lake Washington. Primary statistics from wave measurements revealed a significant wave height ranging from 0.2 to 0.4 m and peak periods ranging from 2 to 2.5 s. The testing occurred at a mean water depth of 40 m.

The field test data and details are documented and available in the field deployment report (Rusch et al., 2025).

4. Numerical model

The numerical model used in this study is based on the time-domain model equation written as:

$$M\ddot{x} = F_{exc}(t) + F_{rad}(t) + F_{diff} + F_{PTO}(t) + F_{HS}(t) + F_{teth}(t) + F_{drag}(t). \quad (1)$$

$\ddot{x}$ is the acceleration vector and M is the mass matrix. F_{exc} is the excitation force of the incident wave, F_{rad} is the radiation force, F_{diff}, is the wave diffraction force, F_{PTO} is the power-take-off force, F_{HS} represents the hydrostatic restoring force, F_{teth} is the tether tension connecting the nacelle and the heave plate, and F_{drag} is viscous force which models the viscous dissipation on the body.

Eq. (1) is calculated in the time domain software ProteusDS (Dynamic Systems Analysis Ltd, 2018), a commercial software which has previously been experimentally validated for WECs and rigid body dynamics by Nicoll et al. (2012), Robertson et al. (2016). The software solves Eq. (1) for all rigid bodies of the WEC in all degrees of freedom, resulting in a coupled system of differential equations.

The forces in Eq. (1) are categorized as either external forces, or hydrodynamic forces. The external forces, originates from the PTO and tether. A key contribution of this work lies in the enhanced modeling of the PTO force.

4.1. Hydrodynamic forces

The hydrodynamic forces includes the wave excitation force, radiation, diffraction force, hydrostatic restoring force, and drag force. The wave diffraction force can be neglected for devices which are small in comparison to the wavelength (Falnes and Kurniawan, 2020). Journee and Massie (2000) classifies a small body as one whose diameter to wavelength ratio is less than 0.1 to 0.2 as is the case with the device used this study. For devices with varying cross-sectional areas, such as the circular waterline cross-section of the nacelle and floats for the WEC used in this study, the hydrodynamic excitation forces exhibit significant nonlinear behavior even in small and flat waves (Penalba et al., 2017). Consequently, this necessitates the adoption of a nonlinear potential flow model where the hydrostatic and incident wave excitation force are calculated using the nonlinear Froude–Krylov force. While the radiation force remains linear and are computed from frequency-dependent coefficients obtained from Boundary Element Method (BEM) software (WAMIT, 2015).

The nonlinear translational and rotational Froude–Krylov forces, respectively, are given as follows:

$$F_{\mathrm{FK}} = -\int_S P(s)\hat{n}(s)\,ds, \quad (2)$$

$$M_{\mathrm{FK}} = -\int_S P(s)\hat{n}(s) \times r(s)\,\mathrm{d}s, \quad (3)$$

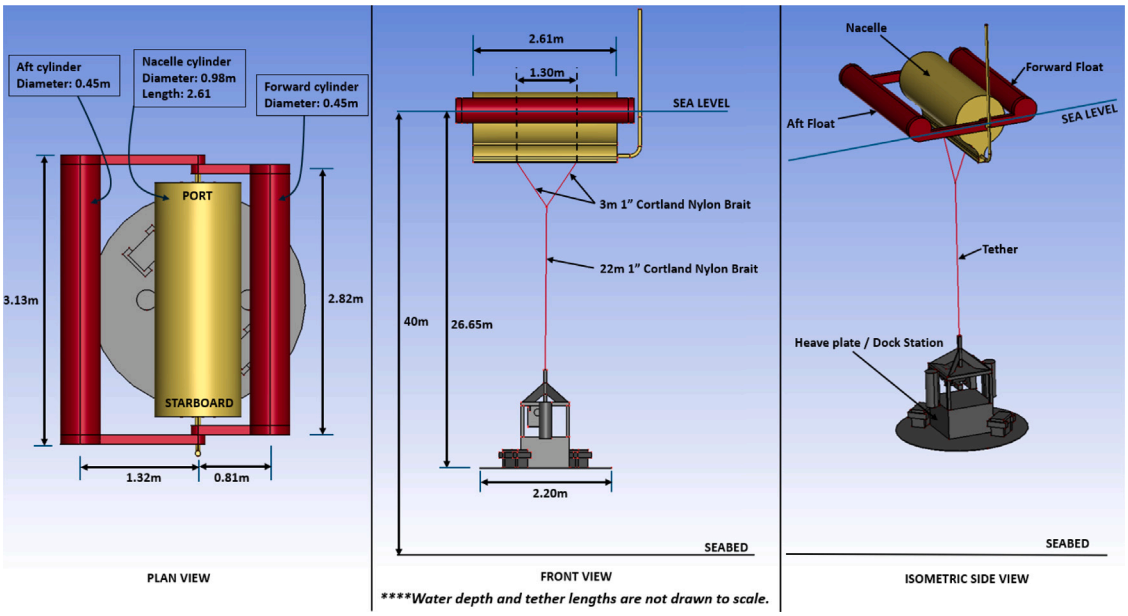

Fig. 1. TigerRAY Schematics.

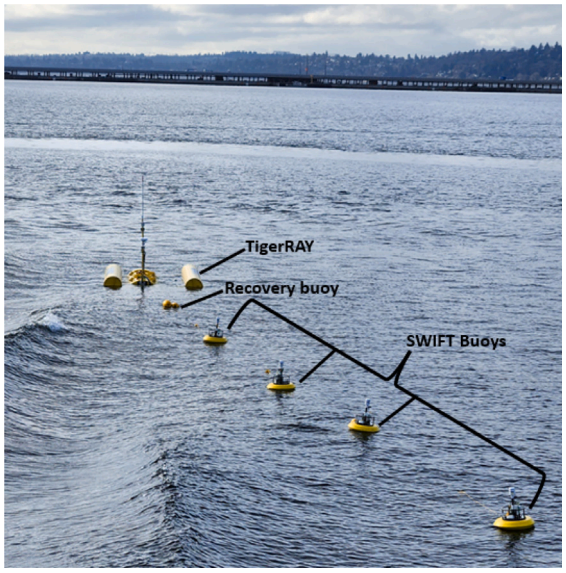

Fig. 2. TigerRAY WEC field deployment.

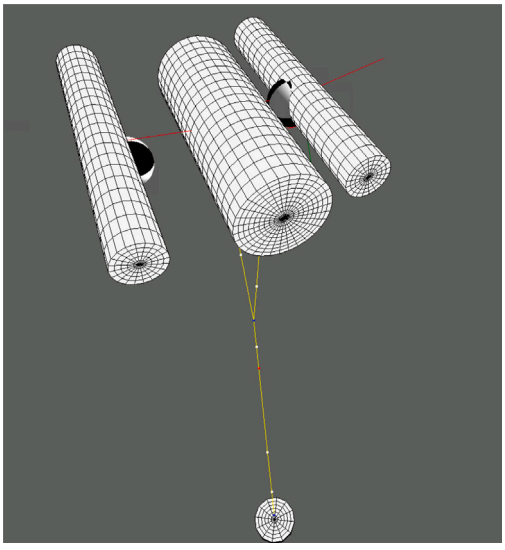

Fig. 3. Cylinder mesh for numerical model.

where S is the entire wetted surface mesh, $\mathrm{d}s$ is the differential area element, $\hat{n}(s)$ is the surface normal at a point s on the surface of the object, and $r(s)$ is the position vector from the pivot point to s. $P(s)$ is the pressure of the fluid at some point s on the surface given as

$$P(s) = \rho g z(s) + \rho \frac{\partial \phi}{\partial t}, \tag{4}$$

where ϕ is first order potential of the incoming wave as described in Dean and Dalrymple (1991), ρ is the density of the fluid, g is the acceleration due to gravity, and $z(s)$ is the depth below the free surface at the point s.

Cylinder geometries are used to prepare the mesh for fore and aft floats, and nacelle as shown in Fig. 3. The mesh specifications for this study are found in Table 1. The reader is further advised to consult Dynamic Systems Analysis Ltd (2018) for more details of the nonlinear Froude–Krylov computation.

The formulation for the radiation force is written as:

$$F_{rad} = A_{\omega}\dot{x}(t) + \int_0^{\infty} B(\tau)\dot{x}(t-\tau)\,\mathrm{d}\tau, \tag{5}$$

where $\dot{x}(t)$ represents the velocity of the body, ω is the frequency, A_{ω} is the hydrodynamic added mass coefficient matrix at infinite frequency, which is derived by evaluating the frequency-dependent hydrodynamic added mass coefficient, $a(\omega)$, at infinite frequency, $(\omega = \infty)$. The term $B(\tau)$ is the radiation memory function, and is written as:

$$B(\tau) = \frac{2}{\pi}\int_0^{\infty} b(\omega)\cos(\omega\tau)\,\mathrm{d}\omega, \tag{6}$$

where $b(\omega)$ represents the frequency-dependent hydrodynamic damping coefficient. The frequency-dependent radiation coefficients are computed by WAMIT, for more details and instructions on the frequency-dependent coefficient calculations, see WAMIT (2015).

Additional viscous damping is incorporated in the time domain model using the Morison equation for quadratic viscous drag force, and

Table 1
Geometric and mesh segments specifications for the float cylinders.

Cylinder	Diameter (m)	Length (m)	# Axial Segments	# Radial Segments	# Angular Segments	Normal drag coefficient
Fore Float	0.45	2.82	18	5	20	1.2
Aft Float	0.45	3.13	20	5	20	1.2
Nacelle	0.98	2.61	18	10	30	1.2

is written as:

$$F_{drag} = \frac{1}{2}\rho C_d A(\dot{x}_b - \dot{x}_f)|\dot{x}_b - \dot{x}_f|, \tag{7}$$

where ρ is the fluid density, C_d is the drag coefficient, A is the projected area in the direction of relative fluid flow, and $\dot{x}_b$ and $\dot{x}_f$ are the velocities of the body and fluid at the centroid, respectively. The fluid velocity are obtained using linear wave potential theory as described in Dean and Dalrymple (1991). Constant drag coefficients available in literature (Det Norske Veritas, 2014) for cylinders, are refined using free decay results and used for the nacelle, forward and aft float and is shown in Table 1. A different drag coefficient was used for the heave plate as explained in Section 4.4. A more detailed explanation of the drag force implementation in the simulation can be found in Dynamic Systems Analysis Ltd (2018).

4.2. Advancements in PTO modeling

This study makes a significant contribution to the PTO modeling by incorporating generator inertia and adopting a power-to-speed relationship, derived from dynamometer testing data. These advancements provide a more accurate representation of PTO dynamics and power output, addressing limitations in conventional PTO modeling approaches.

The TigerRay PTO has several nonlinear behaviors, including cut-in speed/voltage, power electronics (PE) current limit, PE power limit, cut-out speed/voltage, and overvoltage (OV) protection. To maintain computational efficiency, the PTO can be simplified and modeled as a function of the shaft angular velocity, and acceleration which are derivatives of the shaft displacement. The shaft angle displacement, θ, is defined as the relative pitch rotation between the respective float (fore or aft), θ_{float}, and the nacelle, θ_{nacelle}. The shaft angle displacement is written as:

$$\theta = \theta_{\text{float}} - \theta_{\text{nacelle}}. \tag{8}$$

The shaft velocities, ω, are obtained by differentiating the shaft angle displacement:

$$\omega = \frac{\mathrm{d}\theta}{\mathrm{d}t}. \tag{9}$$

The shaft accelerations, α, are obtained by differentiating the shaft velocity:

$$\alpha = \frac{\mathrm{d}\omega}{\mathrm{d}t}. \tag{10}$$

The PTO model is implemented externally and integrated with ProteusDs time-domain software using an Application Program Interface (API) code developed in MATLAB. The PTO force is modeled for freewheel and PTO-engaged modes, as detailed below.

In freewheel mode, the joint forces are modeled as the sum of the inertia torque and frictional torque an written as:

$$F_{\text{PTO}} = I\alpha + \tau_{\text{f}}(\omega), \tag{11}$$

Where, I is the generator's moment of inertia shown in Table 2), and $\tau_{\text{f}}(\omega)$ is the velocity-dependent frictional torque. $\tau_{\text{f}}(\omega)$ is obtained by the interpolation of friction torque to shaft speed relationship shown in Fig. 4.

When the PTO is engaged, both the PTO damping and the PTO friction are characterized together and expressed as a single joint damping term. As shown in Fig. 5, the damping torque exhibits piecewise

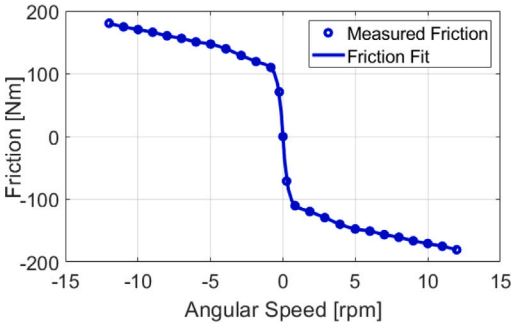

Fig. 4. Frictional Torque as a function of rotation speed for Aft and Fore PTO.

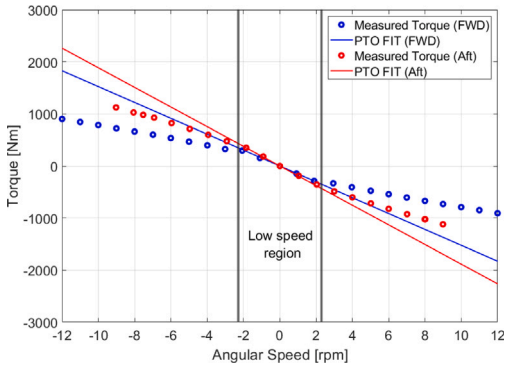

Fig. 5. PTO damping torque as a function of rotation speed for Fore and Aft PTO (Rusch et al., 2023).

Table 2
Details of WEC PTO.

	Aft PTO	Fore PTO
Inertia, I (kg m^2)	106	106
Damping, C_{PTO} (Nms/rad)	−1801.33	−1455.58

behavior as a function of shaft speed. This is a result of the PTO architecture, which contained two different power electronics 'stages' for low and high power conditions (Rusch et al., 2023). The PTO force is modeled using the torque-speed relationship in the low-speed region (−2 rpm to 2 rpm) as described by Rusch et al. (2023) and shown in Fig. 5, as this region accurately represents majority of the conditions in which the WEC is modeled as shown in Figs. 20 and 21.

The equation fit for the PTO force when the PTO is engaged is written as:

$$F_{\text{PTO}} = I\alpha + C_{\text{pto}}\omega, \tag{12}$$

Where, C_{PTO} signifies the PTO damping slope for the low speed region shown in Table 2. An alternative to Eqs. (11) and (12) is to add the PTO generator inertia to the pitch moment of inertia (I_{yy}) of the floats provided in Table 4. Consequently, Eqs. (11) and (12) will have to be updated to solely account for PTO damping terms.

Additionally, a constant static friction of 72 Nm is applied on the both aft and fore shafts for both freewheel and PTO activated mode,

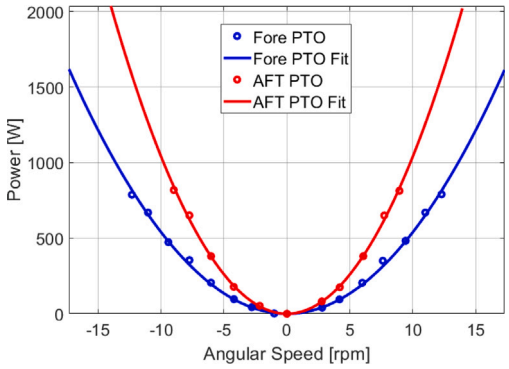

Fig. 6. Power to speed relationship for Fore and Aft PTO.

within a shaft speed range of −0.2 rpm to +0.2 rpm, to mimic the impacts of measured stiction in the PTO.

This study uses a power-speed relationship derived from PTO dynamometer testing data by Rusch et al. (2023) to evaluate the useful power and energy output from the PTO generator in the simulation. This method is chosen because it inherently accounts for inefficiencies in the PTO, providing a more accurate estimate of the useful power output. The power-speed relationship is shown in Fig. 6. The equation fit for the power to speed relationship is written as:

$$P = C_{\text{power}} \cdot \omega^2, \tag{13}$$

where P is the useful power from the PTO generator, C_{power} is the damping slope of the relationship which is $492.5 Nms/rad$ for the fore PTO and $949.2 Nms/rad$ for the aft PTO.

The total energy produced by the WEC over a specified time period T is calculated as:

$$E = \int_0^T P(t)\,dt = \left\{ \frac{1}{T} \int_0^T P(t)\,dt \right\} T \tag{14}$$

where $P(t)$ is the instantaneous useful power output from the PTO generator, dt is the sampling rate or time step, and $\left\{ \frac{1}{T} \int_0^T P(t)\,dt \right\}$ represents the mean or average power.

4.3. Tether force

A cubic-spline lumped mass finite-element model (Buckham, 2003) is used to calculate the tether dynamics in ProteusDS software. The key parameters for modeling a synthetic tether in ProteusDS is the axial rigidity (EA).

Often, the EA value is not directly provided in available technical sheets; however, EA can be calculated from percentage elongation as follows:

$$EA = \frac{100 F_\zeta}{\zeta}, \tag{15}$$

where ζ is the percentage elongation at a percentage applied load relative to the breaking load. F_ζ represents the percentage of the applied load relative to the breaking load, multiplied by the breaking load.

The tether used is a 1 inch Nylon 12 Plait, manufactured by Cortland. The specifications can be found in Cortland (n.d). The hydrodynamic forces on the cable are modeled using the Morison equation, with drag and added mass coefficients obtained from Det Norske Veritas (2014). For more details on the tether/cable model, see Dynamic Systems Analysis Ltd (2018).

Table 3
Heave plate parameters.

Parameter	Value
Mass (kg)	1040
Buoyancy (N)	2894
Projected diameter in heave direction, D (m)	2.2
I_{xx} (kg m^2)	260.24
I_{yy} (kg m^2)	236.26
I_{zz} (kg m^2)	266.36

4.4. Heave plate dynamics

The heave plate is submerged far from the free surface ~27 m, and the Froude–Krylov excitation forces and wave radiation forces can be neglected. Thus, the heave plate hydrodynamic model is developed solely using the Morison equation as described in Rusch et al. (2020). This formulation involves the combination of a drag force, Eq. (7), and inertia force, written as:

$$F_{inertia} = C_a \rho V_{\text{disp}} (\ddot{x}_f - \ddot{x}_b), \tag{16}$$

Where, C_a is the added mass coefficient, ρ is the fluid density, V_{disp} is the volume of fluid displaced by the heave plate estimated from the measured wet weight of the heave plate, $\ddot{x}_f$ is the absolute fluid acceleration at the centroid of the body surface obtained using linear wave potential theory as described in Dean and Dalrymple (1991), and $\ddot{x}_b$ is the body's absolute acceleration at the centroid of the body surface.

Since the body is fully submerged, the projected area A and the displaced volume V_{disp} remain unchanged throughout the simulation. Consequently, the complex heave plate (dock) mesh is simplified to a simple mesh with an equivalent projected area and submerged volume (for computational efficiency). A summary of all the properties of heave plate used in the simulation are shown in Table 3.

The drag and added mass coefficients of the oscillating heave plate solely depend on the non-dimensional Keulegan–Carpenter (KC) number (Rusch et al., 2021). The KC number is given as;

$$KC = \frac{2\pi a}{D}. \tag{17}$$

The added mass and drag coefficients for the heave plate are obtained from Rusch et al. (2021) for a flat plate using a KC number of 0.5. The actual KC number, calculated using the maximum heave plate displacement of 0.04 m measured by the heave plate IMU and a heave plate diameter of 2.2 m, is approximately 0.1. However, since the lowest KC number studied in Rusch et al. (2021) was approximately 0.5, this value was used to obtain the drag and added mass coefficients. The obtained drag coefficient of 9 was used directly in the simulation.

For added mass, the results yield $C_a = 0.85$ at $KC = 0.5$. Since the added mass coefficient calculated by Rusch et al. (2021) uses a spherical reference volume, but ProteusDS uses a reference volume equal to the displaced volume of the heave plate, the C_a used for the simulation must be converted as follows:

$$C_a = \left(0.85 \times \frac{1}{6} \times \pi \times D^3\right) / V_{\text{disp}}. \tag{18}$$

4.5. Wave modeling

SWIFT buoys are used to measure the waves during field deployment of TigerRAY. The SWIFT data products are ensembled in bursts of raw data, at intervals of 720 s (12 min). For each 12 min interval the SWIFT processes wave elevation raw data and calculates the wave statistics and wave spectrum. The Spectral information provided by the SWIFT is used to evaluate the significant wave height, Hs and peak period, Tp and used to fit a JONSWAP spectrum.

The software employs a Deterministic Amplitude Scheme (DAS) as discussed by Mankle et al. (2023), where the phases (ϕ_i) of each

Table 4
Description of mass and inertia properties of floats and nacelle.

	Aft float	Fore float	Nacelle
Mass (kg)	301.43	260.33	874.9
CG_x (m)	−1.118	0.683	0
CG_y (m)	0	0	0
CG_z (m)	−0.107	0.11	0
I_{xx} (kg m^2)	481.87	277.21	708.46
I_{yy} (kg m^2)	78.02	29.84	152.41
I_{zz} (kg m^2)	540.84	288.98	642.54
I_{xy} (kg m^2)	−1.64	−0.83	−0.05
I_{xz} (kg m^2)	8.37	2.38	0.47
I_{yz} (kg m^2)	0.3	0.18	−19.23

wave frequency component are randomly assigned from a uniform distribution over the range $[-\pi, \pi]$. A directional spectrum, $D(\theta)$ is added as described in Dynamic Systems Analysis Ltd (2018).

The instantaneous water surface elevation is reconstructed using a discrete finite number of Airy waves, each with distinct heights, frequencies, and wave spreading headings (Dynamic Systems Analysis Ltd, 2018). The reconstructed water surface elevation, repeats it self after $2\pi/\Delta\omega$ seconds, where $\Delta\omega$ is the discretization between the minimum frequency, $\omega_{\min}$, and the maximum frequency, $\omega_{\max}$, of the spectrum, given as $\Delta\omega = (\omega_{\max} - \omega_{\min})/N$. Therefore a large number of frequency components, N is required to avoid this repetition (Faltinsen, 1993). To mitigate this repetition ProteusDS selects the frequency of each component randomly within the interval $[\omega_i - \Delta\omega/2, \omega_i + \Delta\omega/2]$. Regardless, Faltinsen (1993) recommends a minimum of 1000 frequency component depending on the simulation time.

Although the reconstruction process described does not produce an exact replica of the water surface elevation time series present at the WEC during deployment, it generates a time series with the same statistical properties, which is suitable for model validation (International Towing Tank Conference, 2021).

5. Model validation and calibration

The following subsections describes the field campaign numerical model validation process which is comprised of three sequential steps: a static simulation, a free-decay simulation, and lastly, a full dynamic simulation.

The TigerRAY system's coordinate system and sign convention are illustrated in Fig. 7. The figure shows the system in a 2D body frame, where the x and z axes are in the plane of the page, with the y axis pointing into the page (perpendicular to the x-z plane). The global coordinates are denoted as $[x_G, z_G]$, representing the still waterline as the global reference frame. The local rigid body coordinate frames are defined as $[x_n, z_n]$ for the nacelle, $[x_a, z_a]$ for the aft float, and $[x_f, z_f]$ for the fore float, with the mass properties in Table 4 given relative to these rigid body frames.

The instantaneous translational positions are defined as the positions of the rigid body frames relative to the global reference frame. The rotational positions of the float shafts are described by the angle between the $+x$ axis of each float's rigid body frame and the $-z$ axis of the nacelle.

To ensure consistency, the values used in the comparison were maintained in the same coordinate frame as depicted in Fig. 7 for both simulated and field results. Details on the coordinate system convention of the simulation software can be found in Dynamic Systems Analysis Ltd (2018).

5.1. Static

Static validation serves as a critical step in ensuring the accurate representation of mass properties, hydrostatic buoyancy, and initial body state in the simulation. Additionally, it is used as an input for the dynamic simulation initialization.

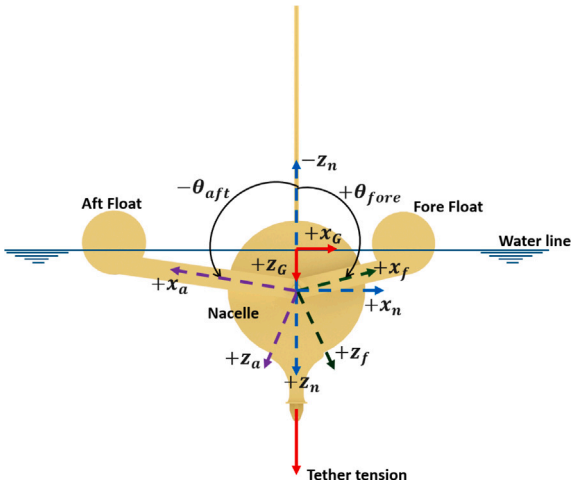

Fig. 7. TigerRAY coordinate reference frame used for model validation.

Table 5
Comparison of Field Measurement and Simulation Static Results.

Parameter	Field measurement	Simulation	% diff
Nacelle waterline (m)	0.325	0.33	1.54
Aft float angle (degrees)	−82	−83.5	1.83
Fore float angle (degrees)	77	79	2.6
Tether tension (N)	7200	7310	1.53

The static validation results are summarized in Table 5, presenting a comparison between simulations and field tests. Field measurements were obtained from February 8th, 2023, when the conditions were calm, with no waves present on the lake. The nacelle waterline, aft and forward float pitch angles, and tether tension were evaluated for agreement between simulation and field data. The comparison shows good agreement, providing confidence in the model representation of static conditions.

5.2. Free decay

A free decay test, where a body is given an initial displacement from equilibrium and released, allowing its motions to decay, was conducted during the field test. This is a common hydrodynamic test that is used to verify validity of hydrodynamic coefficients and forces implemented by Eq. (1) (in the absence of a wave excitation force). During the field decay test, TigerRAY had its heave plate disconnected and the PTO was in freewheel mode. It was released from a height of 0.2 m above the water line and its motion was allowed to decay, as shown in Fig. 8.

The simulation was initialized with the same nacelle position and measured float angles as the field test and ran for 5 s, the duration required for all motions to decay in the field. The free decay test was then used to explore the impact of adding generator inertia into the PTO model. The free decay simulation had two setups; one had PTO inertia included, and the other was without PTO inertia. The free decay test was also used to refine the hydrodynamic drag coefficients for the floats and nacelle. Starting with the drag values provided for a cylinder by Det Norske Veritas (2014), the drag coefficients of the cylinders used for the floats and nacelle were iteratively refined until a close match between the decay response in the field and the simulation was achieved resulting in a refined normal drag coefficient of 1.2.

For the comparison, the simulation data of the nacelle heave, aft float pitch angle, and fore float pitch angle are utilized. Fig. 8 compares the simulation results with and without the inclusion of inertia to the

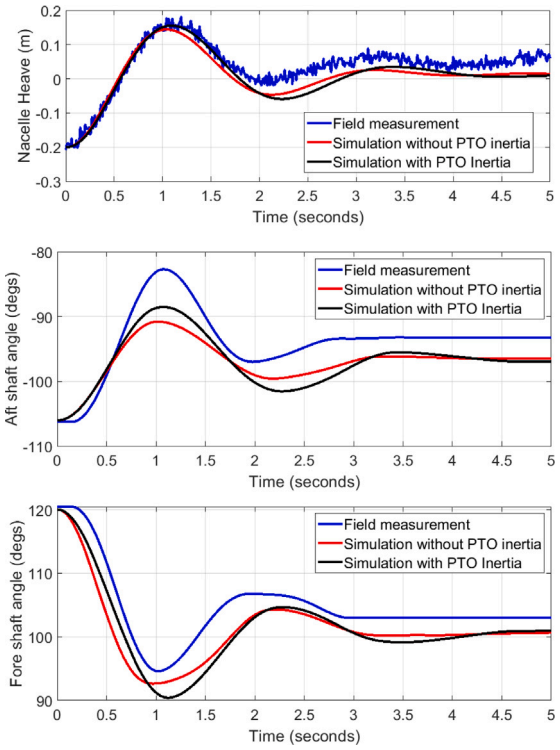

Fig. 8. Comparison of free decay result: (Top) Nacelle heave displacement decay. (Middle) Aft shaft angle displacement decay. (Bottom) Fore shaft angle displacement decay.

Table 6
Comparison of Decay Period and RMSE.

Parameter	Displacement RMSE
Nacelle Heave	
Field	–
sim with PTO inertia (m)	0.035
sim without PTO inertia (m)	0.033
Aft Float	
Field	–
sim with PTO inertia (degrees)	2.83
sim without PTO inertia (degrees)	2.94
Fore Float	
Field	–
sim with PTO inertia (degrees)	3.42
sim without PTO inertia (degrees)	3.96

field data. Both simulations demonstrated reasonable agreement with the field data. However, noticeable differences are likely due to the linear evaluation of radiation coefficients at the mean draft of the cylinders, which does not account for the varying cross-sectional areas along the draft. A nonlinear radiation model could potentially enhance accuracy.

The discrepancies for the free decay comparison are evaluated using the root mean square error (RMSE) between the field and simulated results for nacelle heave, and aft and fore shaft positions. The RMSE values are shown in Table 6.

The results in Table 6 show that the inclusion of inertia in the PTO model resulted in slightly lower RMSE values and slightly improved performance for the simulated aft and fore shaft angle displacements.

6. Results

In this section, the results of the dynamic simulations conducted with the PTO activated and in the presence of waves are presented.

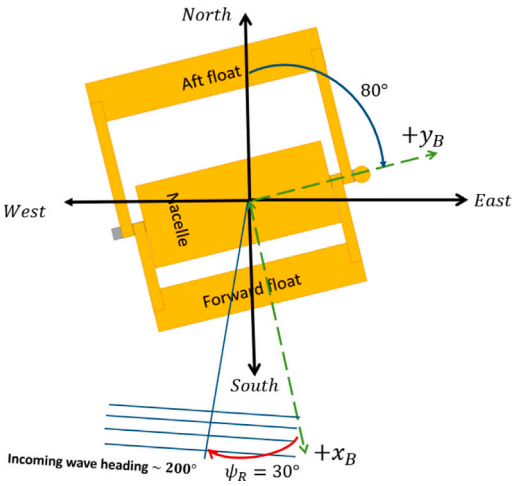

Fig. 9. TigerRAY field orientation.

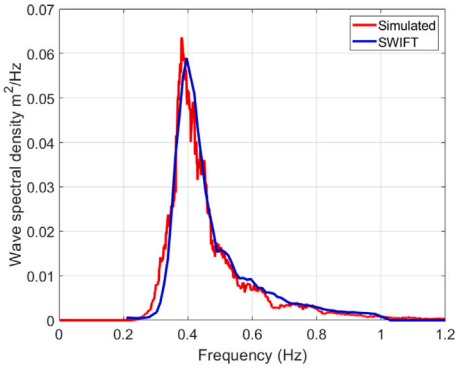

Fig. 10. Comparison between average SWIFT spectral from 21:00:00 to 21:36:00 UTC and simulated wave spectrum.

Table 7
Spectral characteristics for SWIFT and Simulated wave spectral.

	Significant wave height, Hs (m)	Peak period, Tp (s)
SWIFT	0.373	2.52
Simulated	0.371	2.6

Data from the February 6th field test is used for model validation. On this day, the PTO was activated for a continuous duration of 1 h (from 21:00 to 22:00 UTC), corresponding to five measurement intervals for each SWIFT buoy, each 12 min long. The measured SWIFT spectrum were average across the five measurement interval and is used to reconstruct the field waves in the simulation for a duration of 2160s using a JONSWAP spectrum as shown in Fig. 10 and summarized in Table 7. A spectral comparison is first performed to validate if the model accurately simulates the motion dynamics in the field and next a statistical comparison is used to compare the distributions and statistics of the useful power output and shaft speeds. The combination of spectral and statistical comparison provides a more comprehensive validation approach compared to the previous literature validating models with field data (So et al., 2017; Eriksson et al., 2007; Rusch et al., 2022; Leary et al., 2021).

During this time, TigerRAY had an average heading of 80 degrees with a standard deviation of 30 degrees. The peak wave direction was 200 degrees with a standard deviation of 16 degrees. The average heading of TigerRAY and the peak wave direction were used to estimate a relative wave heading of 30 degrees, as shown in Fig. 9.

6.1. Spectral comparison of WEC motion response

By analyzing the energy spectral density of the WEC's motion response, the accuracy of the simulation in replicating the real-world dynamic responses of the system to wave excitation is assessed. This comparison validates the simulation, particularly in capturing the dominant frequencies and the distribution of energy across the frequency spectrum, ensuring that the simulation is a reliable representation of the dynamic response of a WEC, which is crucial for design, optimization, and control (Wilson et al., 2016).

The aft and forward shaft angle displacement responses are the most crucial, as they are directly linked to the energy capture spectrum (ECS) and power performance of TigerRAY. However, for a more elaborate comparison, the responses of all components of TigerRAY are also included in the spectral analysis, including the nacelle heave motion, tether tension, and heave plate heave motion. The spectral analysis was also used to understand how the dynamic response of each component affected each other and also to identify, isolate, and address discrepancies in the numerical model.

A secondary peak was observed between 0.7–0.9 Hz in the spectra of the simulated responses, which is attributed to harmonic excitation of the floats. This occurs in the simulation as the wave spectrum with a short peak period of $T_p = 2.5$ s contains higher-frequency components that overlap with the natural frequency range of the floats, producing a secondary response (harmonic) near resonance. This behavior is consistent with the expected hydrodynamic response when portions of the incident wave spectrum coincide with the body resonance band. The phenomenon was not observed in the field data, likely due to additional damping and signal filtering inherent in the measurement system and post-processing, which tend to suppress higher-frequency harmonic content. For consistency, the secondary peak around 0.7–0.9 Hz was attenuated before statistical comparison to focus the analysis on the dominant physical response observed in the field measurements.

6.1.1. Spectral analysis of nacelle heave motion

The spectral analysis of the nacelle heave displacement presented in Fig. 11 revealed matching peak frequencies at 0.38 Hz (2.63 s) and main energy spectrum bandwidth between 0.25 Hz to 0.65 Hz. However, there is a significant discrepancy in the spectral magnitudes at peak frequencies, with the simulation having a spectral magnitude twice the field spectral.

The discrepancies of spectral magnitudes at peak frequencies could be linked to the overprediction of the resultant hydrodynamic forces on the nacelle cylinder and/or as a result of imperfect modeling of the tether stiffness which transfers the excitation of the nacelle to the heave plate. In reality, the tether dynamic stiffness changes with applied load, while the numerical model used a constant stiffness obtained using the average load experienced. Also, the presence of rigid connectors, such as shackles, present in the field test will result in a greater tether stiffness which were not added in the tether model of the simulation. If the tether's overall stiffness is underestimated compared to the actual field setup, the nacelle will exhibit greater motion also leading to lower tether tension in the simulation compared to field measurements.

6.1.2. Spectral analysis of fore shaft angle displacement

The spectral analysis of the fore shaft angle displacement revealed good agreement as shown in Fig. 12. The peak frequencies are almost identical, with the field data having a peak frequency of 0.38 Hz (2.63 s) and the simulated data having a peak frequency of 0.377 Hz (2.65 s). The spectral magnitudes at the peak frequency were also closely matched. Furthermore, the distribution of energy across frequencies aligned quite well with main energy occurring from 0.3 Hz to 0.7 Hz for both field and simulated data, representing the device's energy capture spectrum for the exciting wave condition.

As discussed earlier in Section 6.1, a secondary peak between 0.7 Hz and 0.9 Hz was evident in the simulated fore shaft displacement response spectrum and appeared more pronounced in the shaft speed (see Fig. 13), which would have resulted in higher simulated shaft speeds and, consequently, higher predicted power output compared to the field data. For consistency, this secondary component was attenuated prior to statistical comparison to focus the comparison on the dominant physical response observed in the field measurements.

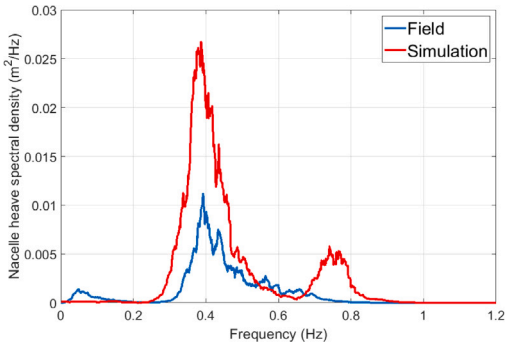

Fig. 11. Spectral density functions for nacelle heave displacement.

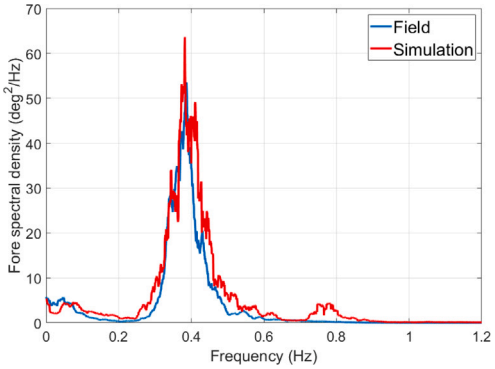

Fig. 12. Spectral density functions of the fore shaft displacement.

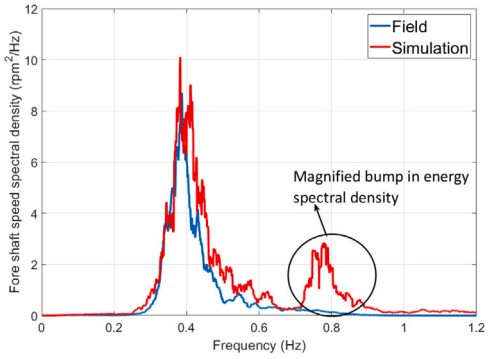

Fig. 13. Spectral density functions of the fore shaft speed.

6.1.3. Spectral analysis of aft shaft angle displacement

The spectral analysis of the aft shaft angle displacement, presented in Fig. 14, also shows excellent consistent spectral behavior in terms of validating peak frequencies and energy distribution, and matching spectral magnitudes at peak frequency. The secondary peak between 0.7–0.9 Hz was also evident in the simulated aft shaft displacement and appeared more pronounced in the shaft speed (see Fig. 15), which would have resulted in higher simulated shaft speeds and, consequently, higher predicted power output compared to the field data. For consistency, this secondary component was also attenuated prior to statistical comparison to focus the comparison on the dominant physical response observed in the field measurements.

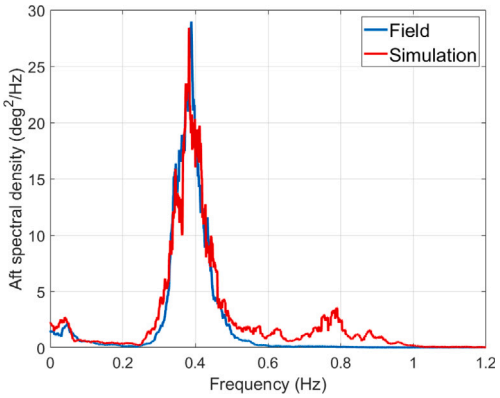

Fig. 14. Spectral density functions of the aft shaft displacement.

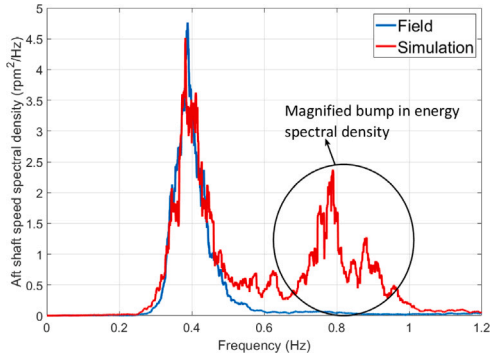

Fig. 15. Spectral density functions of the aft shaft speed.

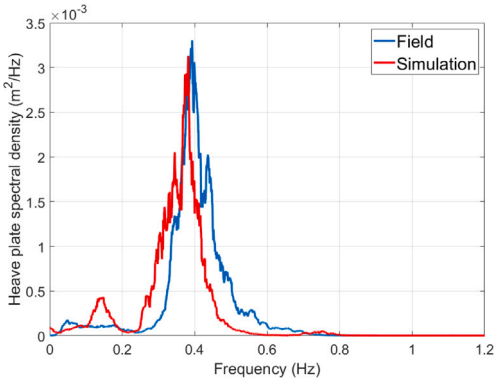

Fig. 16. Spectral density functions for heave plate heave displacement.

6.1.4. *Spectral analysis of heave plate heave motion*

The spectral analysis of the heave plate heave displacement presented in Fig. 16 also shows good agreement, particularly in the magnitude of response. A slight discrepancy was observed in the peak frequencies, with the simulation having a peak frequency of 0.363 Hz (2.75 s) compared to the field data with a peak frequency of 0.38 Hz (2.63 s). This resulted in a slight shift of the energy distribution to the lower frequency side. The frequency discrepancies in spectral analysis of the heave plate heave displacement could be attributed to a simplification of the heave plate geometry, which converts the complex heave plate geometry to a cylinder of equivalent projected diameter and submerged volume. Also, uncertainties arising from the selection of a single drag and added mass coefficient, instead of a KC-dependent value (Rusch et al., 2021) will also create some sources of discrepancies to the model.

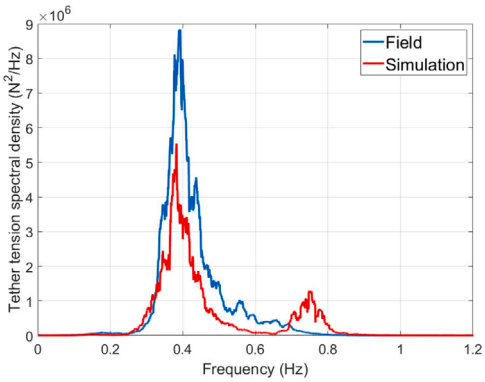

Fig. 17. Spectral density functions for tether tension.

6.1.5. *Spectral analysis of tether tension*

The dynamic tension of the tether is isolated by subtracting the mean static tension from the tether tension data for both the field and simulation. This dynamic tether tension should be equivalent to the resultant hydrodynamic forces on the nacelle and heave plate, since the tether is used to transfer the resultant dynamic force of the nacelle to the heave plate.

The spectral analysis of the tether tension, presented in Fig. 17, shows that the simulation accurately captured the peak frequency of the field spectrum, as well as matching the distribution of energy across the frequency spectrum from 0.3 Hz to 0.6 Hz. The major discrepancy in the spectral comparison was the mismatch in the spectral magnitude of the spectrum at the peak frequency, with the simulation having a lesser spectral magnitude than the field spectrum at the peak frequency.

The lower dynamic tension in the simulation is likely as a result of underprediction of resultant hydrodynamic force between the nacelle and heave plate in the simulation. As stated in the results of the nacelle heave spectral, Section 6.1.1, the discrepancy is also likely due to the imperfection in representing the tether stiffness in the model. Furthermore, the linearization of the radiation force will also introduce sources of discrepancy in the resultant hydrodynamic force.

6.2. *Statistical comparison of power and shaft speed*

The statistical comparisons provides a complementary evaluation of the accuracy of the simulation in replicating trends, variability, average values, and percentiles of the power performance measured in the field. Fig. 18 and Fig. 19 present histograms of the forward and aft PTO generator power output, respectively, comparing the simulation results with field measurements. Each histogram bin represents a 1 W increment, allowing for a detailed view of the distribution across the power range. The simulation and field distributions align closely. The probability of occurrence steadily decreases with increasing power output. The histograms are truncated at 40 W, as power levels beyond this range occurred with a probability below 0.1%, and were excluded for clarity.

To better understand the PTO power probability distribution, the distribution of PTO shaft speed time history for both field data and simulation is investigated and compared. The shaft speed histograms shown in Figs. 20 and 21, exhibited a similar trend to the power probability distribution.

The statistical metrics presented in Tables 8–10 provide quantitative insights into the WEC's power performance and energy production over the 36-minute analysis period. The mean represents the average power output over time, while the standard deviation quantifies fluctuations due to wave variability. The 5th and 95th percentiles capture the distribution tails, reflecting low- and high-power production thresholds.

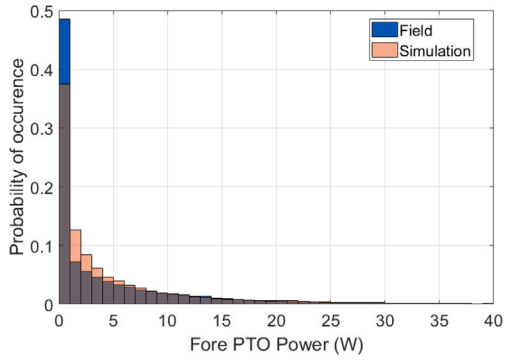

Fig. 18. Probability distribution comparison for fore PTO generator power output. (The gray areas indicate regions where the probability distributions of field and simulation data overlap.)

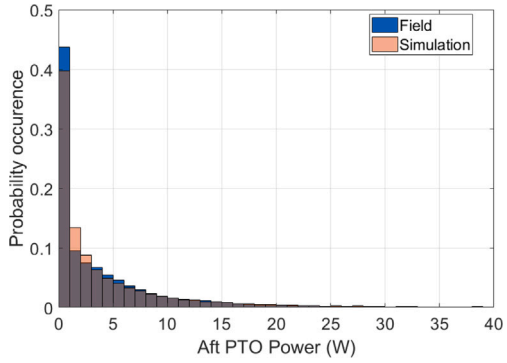

Fig. 19. Probability distribution comparison for aft PTO generator power output.(The gray areas indicate regions where the probability distributions of field and simulation data overlap.)

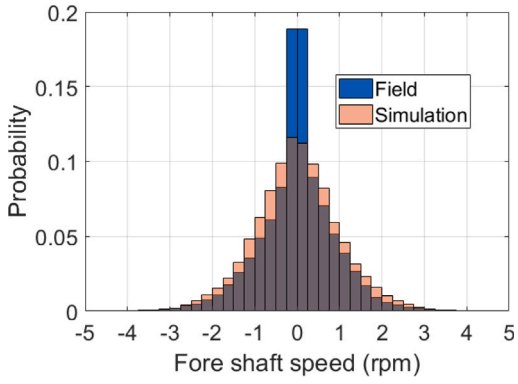

Fig. 20. Probability distribution comparison for fore shaft speed. (The gray areas indicate regions where the probability distributions of field and simulation data overlap.)

These comparisons revealed a close match to the simulated and field results, further quantified using the percentage difference calculation:

$$\%\,\text{diff} = \frac{|V_1 - V_2|}{\left(\frac{V_1 + V_2}{2}\right)} \times 100 \tag{19}$$

where V_1 and V_2 are the field and simulated values, in any order.

In Table 8 and 9, the mean power output for both the fore and aft PTOs shows a percentage difference of 9.16% and 9.13%, respectively, indicating that the model closely predicts the average power output

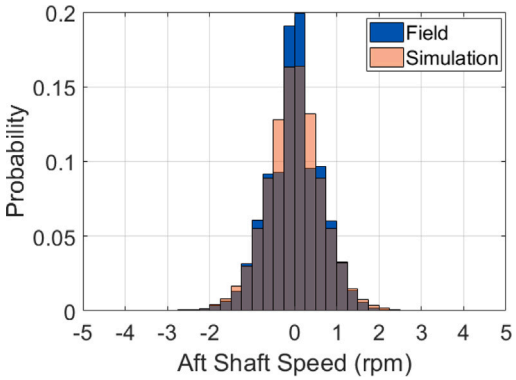

Fig. 21. Probability distribution comparison for aft shaft speed. (The gray areas indicate regions where the probability distributions of field and simulation data overlap.)

Table 8
Statistical comparison of fore PTO generator power from field measurements and numerical simulation.

Statistic	Field (W)	Simulation (W)	%diff
Mean	6.05	5.52	9.16%
Standard Deviation	12.11	10.22	16.92%
5th Percentile	0.00	0.00	–
95th Percentile	23.00	22.78	0.96%

Table 9
Statistical comparison of aft PTO generator power from field measurements and numerical simulation.

Statistic	Field (W)	Simulation (W)	%diff
Mean	4.18	4.58	9.13%
Standard Deviation	7.00	7.90	14.21%
5th Percentile	0.00	0.00	–
95th Percentile	17.12	18.31	6.67%

Table 10
Total useful energy produced by fore and aft PTO generator in a 36 min duration.

Aft PTO Statistic	Field (J)	Simulation (J)	% Difference
Fore PTO	12,990	11,898	8.77%
Aft PTO	9,021	9,903	9.32%

across the simulation duration. Table 10 extends this evaluation by considering the total useful energy produced over a 36-minute duration. Here, the percentage differences remain similarly low, with 8.77% for the fore PTO and 9.32% for the aft PTO. These results demonstrate strong alignment between the simulated and field-measured performance and further validate the model's ability to replicate the overall power and energy generation trends observed in the field.

7. Discussion

This section discusses the challenges and limitations encountered during development and validation of the novel numerical model (when comparing against field data), the implications of PTO modeling methodology, and the significance of applying a more detailed validation approach, such as spectral validation. Additionally, it covers the sensitivity of the numerical model, highlighting key lessons learned from the numerical modeling and validation exercise.

7.1. Limitations and difficulties in model validation

The main challenge for the development and validation of numerical models, using field deployment data, is the lack of wave elevation records at the WEC location. This prevents exact time series comparisons, necessitating the use of statistical and spectral analysis. Currently, measuring the wave elevation at the exact WEC location during field testing is unrealistic/impossible as the WEC obstructs the measurement and alters the wave height itself. However, recent developments in phase-resolved wave prediction and reconstruction, as described in Fisher et al. (2021), offer promising avenues for detailed direct time series comparison. This approach was attempted within this work but proved ineffective due to the presence of short wind waves. An alternative approach could involve using pressure sensors on the heave plate or WEC body to estimate wave elevation at the free surface using potential dynamic pressure formulation (Jones and Monismith, 2007).

The model was implemented using a partially nonlinear potential flow formulation, in which the hydrostatic and incident wave excitation forces were computed using nonlinear Froude–Krylov integration over the instantaneous wetted surface, while the radiation force remained linear. Potential flow theory neglects viscous effects; however, these were incorporated through a Morison-type quadratic drag formulation. The linear evaluation of radiation forces relies on frequency-dependent added-mass and damping coefficients computed at the mean draft and orientation of the floating body. This linearization assumes small-amplitude motions and constant wetted and waterplane areas. For the spherical floats cross-section considered in this study, the geometry itself causes the waterplane and wetted areas to vary with draft, and these variations are further amplified by the relatively large pitch motions occurring during power generation. As a result, the true added mass and radiation damping vary with the instantaneous draft and orientation, effects that are not fully captured by the linear coefficients. Despite these limitations, the model successfully reproduced the dominant dynamic response and power performance observed in field tests with good agreement.

An average wave heading of 80 degrees for the device was used in this study to represent the relative heading. However, the device exhibited a yaw drift with a standard deviation of 16 degrees during the field deployment. Additionally, the wave direction of 200 degrees, used to calculate the relative wave heading as shown in Fig. 9, represents the peak wave direction, rather the full spread of directions with time. Instantaneous wave direction was not accounted for, creating a potential significant mismatch in the relative instantaneous wave heading between the field and the simulation. This effect can be attributed for some of the discrepancy between the spectral analyses of the simulated and field data.

7.2. Significance of spectral validation

Incorporating spectral analysis into the comparison of wave energy converter field and simulation data provides a more complete understanding of the dynamic behavior of the system, extending beyond the scope of traditional statistical methods utilized in the current literature for WEC numerical to field data validation.

This approach has proven invaluable in refining the dynamic model of the WEC. By analyzing the energy spectral density of various system components of the WEC, it becomes possible to identify specific areas where simulation inaccuracies arise and to pinpoint which aspects of the model require refinement. For instance, in a system with multiple components and complex interactions, such as the TigerRAY WEC, spectral analysis provided critical insights that were not immediately apparent from raw time series data alone.

A key example of this is the spectral analysis of the nacelle's motion response, which initially indicated a higher response in the simulation compared to the field data. Without spectral analyses, one might have inferred that this was due to an overestimation of the resultant hydrodynamic forces acting on the nacelle. However, a closer examination of the tether's dynamic tension, corresponding to the resultant hydrodynamic force, reveals that the simulation actually exhibited lower tension response at the peak frequency. This suggested an underestimation of the resultant hydrodynamic forces between the nacelle and heave plate.

This counterintuitive finding led to a revised inference: the higher simulated motion response of the nacelle was more likely due to inaccuracies in modeling the tether stiffness, rather than an overestimation of resultant hydrodynamic forces. An inaccurate representation in the form of underestimating the tether stiffness would result in more tether elongation, preventing the effective transfer of tension from the nacelle excitation to the heave plate and allowing more heave motion of the nacelle.

The presence of an additional load cell at the nacelle connection end of the tether during field deployments would have helped for the isolation of the hydrodynamic forces acting separately on the nacelle and the heave plate. Meanwhile, adding methods to measure tether elongation, such as fiber optics and strain gauges, would have provided more definitive data on the tether stiffness. These improvements could have further refined the model and helped narrow down the potential sources of discrepancies related to the interaction of forces. Additionally, prior bench-testing of the tether's dynamic stiffness would have provided valuable input for the numerical model.

These insights underscore the importance of spectral analysis as a critical tool for identifying and correcting discrepancies in the dynamic model.

7.3. Implications of PTO model

The free decay results shown in Fig. 8 revealed that including PTO inertia in the model had limited impact on the motion dynamics of either the aft or forward shaft for this particular WEC scale. However, this is expected to be specific to the case-study WEC. For larger PTO generator with higher inertia and more energetic seastate creating larger shaft accelerations the effect of generator inertia will likely be significant.

Using the power-to-shaft-speed relationship (obtained from dynamometer testing data), produces more realistic power outputs, when compared to the conventional method of multiplying the PTO force by shaft speed. The latter approach would have resulted in significantly higher average power outputs, as shown in Table 11. The damping slopes for the power-to-speed relationship, Fig. 6, revealed that the value for the fore PTO (492.5 Nms/rad) was approximately one-third of the slope of the optimal PTO damping, Fig. 5, (1455 Nms/rad). Similarly, for the aft PTO, the damping slope (949 Nms/rad) from the power-to-speed relationship was approximately half of the optimal damping value (1801 Nms/rad). This outcome was expected as not all of the applied damping will be transformed to useful power, due to loses from heat, friction, and other generator inefficiencies. The power to speed relationships helps to map the generator shaft speed to useful PTO power accounting for all forms of possible losses and inefficiencies. This highlights the importance of PTO dynamometer and bench testing prior to testing and validation of full-scale WECs.

7.4. Sensitivity of numerical model

The numerical model's sensitivity was evident when subjected to varying environmental conditions. Wave direction played a significant role in the motion dynamics. During model initialization, when waves approached the device at zero degree through the fore float, the fore shaft experienced greater rotation than the aft shaft. Conversely, when waves approached through the aft float, the aft shaft had larger rotations. This phenomenon was noteworthy, but beyond the scope of this study. It remains unclear how wave direction affects the overall total

Table 11
Significance of PTO power output implementation.

Parameter	Fore PTO (W)	Aft PTO (W)
Field	6.05	4.18
Numerical: Power-speed relationship	5.52	4.58
Numerical: PTO force multiplied by shaft speed	20.86	11.66

power output performance of the WEC and this is suggested as a future research direction.

The components of the device itself also influenced the model's sensitivity, particularly the stiffness of the tether. During initial model runs and dynamic simulation initialization, it was observed that a stiffer tether reduced the motion of the nacelle, consequently affecting the rotation of the shafts. The heave plate weight and reaction force also affected the response dynamics. Additionally, the ratio of aft to fore float lever arm could play a role in the overall device performance. A comprehensive evaluation of the sensitivity and how the various components of the WEC affect performance was beyond the scope of this work. Therefore, a numerical study using this validated model should be performed to ascertain how these factors influence the overall performance of the WEC, providing avenues for future research.

8. Conclusions

The development and validation of numerical simulation, based on real-world field deployment data requires a unique set of approaches to effectively validate the dynamics and performance of WECs. This study successfully utilized real-world field testing data to develop and validate a numerical model of a WEC with tethered heave plate WEC. The validation combined statistical and spectral analysis, which provided deeper insights into the model's ability to capture the coupled WEC motion dynamics accurately compared to previous validation attempts with field data. The simulation results showed good agreement with the field data. Further discrepancies were likely attributed to known inaccuracies and simplifications in PTO, modeling tether forces, the resultant hydrodynamic force on the nacelle, and linearization of radiation forces. The spectral comparison provided initial insights on the numerical model ability to predict the observed dominant dynamic responses, and the statistical analysis revealed a close alignment between the field and simulated power outputs and total energy produced, with a percentage difference approximately 9% for the mean power output and total energy across both PTOs. Higher fidelity numerical models are suggested to address further discrepancies. Spectral analysis played a crucial role in identifying these areas of discrepancy, underscoring the importance of its use alongside statistical analysis in validation of numerical models using field data.

As a future recommendation for field deployments of multi-body WECs with tethered heave plates, incorporating additional sensors, such as a load cell at the nacelle connection and methods for measuring tether elongation like fiber optics or strain gauges, would provide more comprehensive data. These enhancements would help refine the model and reduce the potential sources of discrepancies in the interaction of forces.

This study also identified gaps in incorporating generator inertia into PTO models and the overestimation of power output using conventional methods. It developed a framework for including generator inertia and introduced a more realistic power prediction approach. While inertia had limited effects for this WEC scale and wave condition, it could be significant for larger WECs and larger wave conditions. Using a power-to-speed relationship from dynamometer testing data provided more accurate power predictions, highlighting the importance of integrating this method into WEC models for realistic performance evaluation.

Finally, the study demonstrated the effectiveness of field testing for validating WEC performance, especially for complex WEC systems that are difficult to replicate in scaled wave tanks. The methods used in this study provides a practical guideline for WEC developers and researchers seeking to validate WEC numerical models or compare them against field test data enhancing the accuracy of numerical models and advancing WEC technology development.

CRediT authorship contribution statement

David Okushemiya: Writing – original draft, Validation, Methodology. **Curtis J. Rusch:** Writing – review & editing, Supervision. **Bryson Robertson:** Writing – review & editing, Supervision, Funding acquisition. **Zhe Zhang:** Writing – review & editing.

Declaration of competing interest

The authors declare that they have no known competing financial interests or personal relationships that could have appeared to influence the work reported in this paper.

Acknowledgments

This research is supported by Naval Facilities Engineering Systems Command (NAVFAC) (via Naval Sea Systems Command (NAVSEA)) contract number: N0002410D6318-N0002419F8709. The authors would also like to thank Jim Thomson, Erik Hammagren and Corey Crisp, for their support during the field deployment campaign.

References

American Bureau of Shipping, 2021. Guidance notes on the application of fiber rope for offshore mooring. URL: https://ww2.eagle.org/content/dam/eagle/rules-and-guides/current/offshore/90_fiberrope_2021/fiber-rope-gn-june21.pdf.

Bacelli, G., Spencer, S.J., Patterson, D.C., Coe, R.G., 2019. Wave tank and bench-top control testing of a wave energy converter. Appl. Ocean Res. 86, 351–366. http://dx.doi.org/10.1016/j.apor.2018.09.009.

Beatty, S., Ferri, F., Bocking, B., Kofoed, J.P., Buckham, B., 2017. Power take-off simulation for scale model testing of wave energy converters. Energies 10, http://dx.doi.org/10.3390/en10070973.

Beatty, S.J., Hall, M., Buckham, B.J., Wild, P., Bocking, B., 2015. Experimental and numerical comparisons of self-reacting point absorber wave energy converters in regular waves. Ocean Eng. 104, 370–386. http://dx.doi.org/10.1016/j.oceaneng.2015.05.027.

Buckham, B.J., 2003. Dynamics Modelling of Low-Tension Tethers for Submerged Remotely Operated Vehicles (Doctoral dissertation). Department of Mechanical Engineering, University of Victoria.

Chen, M., Vivekanandan, R., Rusch, C.J., Okushemiya, D., Manalang, D., Robertson, B., Hollinger, G.A., 2024. A unified simulation framework for wave energy powered underwater vehicle docking and charging. Appl. Energy 361, 122877. http://dx.doi.org/10.1016/j.apenergy.2024.122877.

Cheng, Y., Fu, L., Dai, S., Collu, M., Cui, L., Yuan, Z., Incecik, A., 2022a. Experimental and numerical analysis of a hybrid wec-breakwater system combining an oscillating water column and an oscillating buoy. Renew. Sustain. Energy Rev. 169, 112909. http://dx.doi.org/10.1016/j.rser.2022.112909.

Cheng, Y., Fu, L., Dai, S., Collu, M., Ji, C., Yuan, Z., Incecik, A., 2022b. Experimental and numerical investigation of wec-type floating breakwaters: A single-pontoon oscillating buoy and a dual-pontoon oscillating water column. Coast. Eng. 177, 104188. http://dx.doi.org/10.1016/j.coastaleng.2022.104188.

Cheng, Y., Liu, W., Dai, S., Yuan, Z., Incecik, A., 2024. Wave energy conversion by multi-mode exciting wave energy converters arrayed around a floating platform. Energy 313, 133621. http://dx.doi.org/10.1016/j.energy.2024.133621.

Cheng, Y., Xi, C., Dai, S., Ji, C., Collu, M., Li, M., Yuan, Z., Incecik, A., 2022c. Wave energy extraction and hydroelastic response reduction of modular floating breakwaters as array wave energy converters integrated into a very large floating structure. Appl. Energy 306, 117953. http://dx.doi.org/10.1016/j.apenergy.2021.117953.

Coe, R.G., Bacelli, G., Wilson, D.G., Abdelkhalik, O., Korde, U.A., Robinett III, R.D., 2017. A comparison of control strategies for wave energy converters. Int. J. Mar. Energy 20, 45–63. http://dx.doi.org/10.1016/j.ijome.2017.11.001.

Cortland, (n.d), Nylon 12 plait rope. URL: https://www.cortl{andc}ompany.com/all-rope/#nylon-12-plait.

Czech, B., Bauer, P., 2012. Wave energy converter concepts : Design challenges and classification. IEEE Ind. Electron. Mag. 6, 4–16. http://dx.doi.org/10.1109/MIE.2012.2193290.

Darwish, A., Aggidis, G.A., 2022. A review on power electronic topologies and control for wave energy converters. Energies 15, http://dx.doi.org/10.3390/en15239174.

Dean, R.G., Dalrymple, R.A., 1991. Water Wave Mechanics for Engineers and Scientists. vol. 2, World Scientific Publishing Company.

Dessi, D., Passacantilli, F., Leonardi, G., 2022. Experimental and numerical modeling of a piezoelectric floating system for wave energy harvesting. Appl. Ocean Res. 122, 103120. http://dx.doi.org/10.1016/j.apor.2022.103120.

Det Norske Veritas, 2014. Recommended practice dnv-rp-c205: Environmental conditions and environmental loads.

Dynamic Systems Analysis Ltd, (2018), ProteusDS v2.45 Manual. URL: https://proteusds.com/documentation/.

Eriksson, M., Waters, R., Svensson, O., Isberg, J., Leijon, M., 2007. Wave power absorption: Experiments in open sea and simulation. J. Appl. Phys. 102.

Falnes, J., Kurniawan, A., 2020. Ocean waves and oscillating systems: Linear interactions including wave-energy extraction. In: Cambridge Ocean Technology Series, second ed. vol. 8, Cambridge University Press, United Kingdom, http://dx.doi.org/10.1017/9781108674812.

Faltinsen, O., 1993. Sea Loads on Ships and Offshore Structures. vol. 1, Cambridge University Press.

Fisher, A., Thomson, J., Schwendeman, M., 2021. Rapid deterministic wave prediction using a sparse array of buoys. Ocean Eng. 228, 108871. http://dx.doi.org/10.1016/j.oceaneng.2021.108871.

Fitzgerald, J., Bergdahl, L., 2008. Including moorings in the assessment of a generic offshore wave energy converter: A frequency domain approach. Mar. Struct. 21, 23–46. http://dx.doi.org/10.1016/j.marstruc.2007.09.004.

Freeman, M.C., O'Neil, R., Garavelli, L., Hellin, D., Klure, J., 2022. Case study on the novel permitting and authorization of pacwave south, a us grid-connected wave energy test facility: Development, challenges, and insights. Energy Policy 168, 113141. http://dx.doi.org/10.1016/j.enpol.2022.113141.

Gaudin, C., Lowe, R., Draper, S., Hansen, J., Wolgamot, H., O'Loughlin, C., Fievez, J., Taylor, D., Pichard, A., 2018. A wave energy research centre in albany, australia. In: Proceedings of the 4th Asian Wave and Tidal Energy Conference. AWTEC 2018.

Giannini, G., Temiz, I., Rosa-Santos, P., Shahroozi, Z., Ramos, V., Göteman, M., Engström, J., Day, S., Taveira-Pinto, F., 2020. Wave energy converter power take-off system scaling and physical modelling. J. Mar. Sci. Eng. 8 (632).

Guo, B., Ringwood, J., 2021. A review of wave energy technology from a research and commercial perspective. Renew. Power Gener. IET 15, 3065. http://dx.doi.org/10.1049/rpg2.12302.

Han, Z., Cao, F., Hann, M., Gong, H., Liu, S., Li, M., Shi, H., 2021. Study on the capture spectrum of wave energy conversion. Appl. Ocean Res. 111, 102654. http://dx.doi.org/10.1016/j.apor.2021.102654.

Heller, V., 2011. Scale effects in physical hydraulic engineering models. J. Hydraul. Res. 49, 293–306. http://dx.doi.org/10.1080/00221686.2011.578914.

Hong, Y., Waters, R., Boström, C., Eriksson, M., Engström, J., Leijon, M., 2014. Review on electrical control strategies for wave energy converting systems. Renew. Sustain. Energy Rev. 31, 329–342. http://dx.doi.org/10.1016/j.rser.2013.11.053.

International Towing Tank Conference, 2021. Wave energy converter model test experiments. ITTC Recommended Procedures and Guidelines 7.5-02-07-03.7. In: Specialist Committee on Testing of Marine Renewable Devices of the 29th ITTC. URL: https://www.ittc.info/media/9745/75-02-07-037.pdf.

Jin, S., Greaves, D., Wave energy in the UK: Status review and future perspectives. Renew. Sustain. Energy Rev. 143, 110932. http://dx.doi.org/10.1016/j.rser.2021.110932.

Jin, S., Wang, D., Hann, M., Collins, K., Conley, D., Greaves, D., 2023. A designed two-body hinged raft wave energy converter: From experimental study to annual power prediction for the emec site using wec-sim. Ocean Eng. 267, 113286. http://dx.doi.org/10.1016/j.oceaneng.2022.113286.

Jones, N.L., Monismith, S.G., 2007. Measuring short-period wind waves in a tidally forced environment with a subsurface pressure gauge. Limnol. Ocean.: Methods 5, 317–327. http://dx.doi.org/10.4319/lom.2007.5.317.

Journee, J., Massie, W., 2000. Offshore hydromechanics. TU delft.

Leary, M., Rusch, C., Zhang, Z., Robertson, B., 2021. Comparison and validation of hydrodynamic theories for wave energy converter modelling. Energies 14 (3959), http://dx.doi.org/10.3390/en14133959.

Lesemann, A.R., 2020. Power at sea: Use of wave energy converters for powering offshore oil and gas operations. In: OTC Offshore Technology Conference Day 4 Thu, May 07 2020, D041S052R004. http://dx.doi.org/10.4043/30914-MS.

Li, N., Cheung, K.F., 2014. Wave Energy Resource Characterization at the U.S. Navy Wave Energy Test Site and Other Locations in Hawaii. Technical Report, Hawaii National Marine Renewable Energy Center, URL: https://www.hnei.hawaii.edu/wp-content/uploads/Wave-Energy-Resource-Characterization.pdf.

Mankle, H., Branson, P., DuPont, B., Robertson, B., 2023. Temporal upsampling of wave parameters and impact on time-domain floating body response and wave power. J. Ocean. Eng. Mar. Energy 9, 1–16. http://dx.doi.org/10.1007/s40722-023-00292-z.

Muliawan, M.J., Gao, Z., Moan, T., 2013. Analysis of a two-body floating wave energy converter with particular focus on the effects of power take-off and mooring systems on energy capture. J. Offshore Mech. Arct. Eng. 135, http://dx.doi.org/10.1115/1.4023796.

Nicoll, R.S., Wood, C.F., Roy, A.R., 2012. Comparison of physical model tests with a time domain simulation model of a wave energy converter. In: International Conference on Offshore Mechanics and Arctic Engineering Volume 7: Ocean Space Utilization; Ocean Renewable Energy. pp. 507–516. http://dx.doi.org/10.1115/OMAE2012-83699.

Norris, J., Droniou, E., 2007. Update on emec activities, resource description, and characterisation of wave-induced velocities in a tidal flow. In: Proc. 7th European Wave and Tidal Energy Conference. Porto, Portugal.

Paduano, B., Giorgi, G., Gomes, R.P., Pasta, E., Henriques, J.C., Gato, L.M., Mattiazzo, G., 2020. Experimental validation and comparison of numerical models for the mooring system of a floating wave energy converter. J. Mar. Sci. Eng. 8 (565).

Palm, J., Eskilsson, C., Bergdahl, L., Bensow, R.E., 2018. Assessment of scale effects, viscous forces and induced drag on a point-absorbing wave energy converter by cfd simulations. J. Mar. Sci. Eng. 6, http://dx.doi.org/10.3390/jmse6040124.

Pecher, A., 2017. Experimental Testing and Evaluation of WECs. Springer International Publishing, Cham, pp. 221–260. http://dx.doi.org/10.1007/978-3-319-39889-1_9, chapter 9.

Pedersen, H., Hansen, R., Hansen, A., Andersen, T., Bech, M., 2016. Design of full scale wave simulator for testing power take off systems for wave energy converters. Int. J. Mar. Energy 13, 130–156. http://dx.doi.org/10.1016/j.ijome.2016.01.005.

Penalba, M., Giorgi, G., Ringwood, J., 2017. Mathematical modelling of wave energy converters: A review of nonlinear approaches. Renew. Sustain. Energy Rev. 78, 1188–1207. http://dx.doi.org/10.1016/j.rser.2016.11.137.

Rao, M.J., Nallayarasu, S., Bhattacharyya, S., 2021. Numerical and experimental studies of heave damping and added mass of spar with heave plates using forced oscillation. Appl. Ocean Res. 111, 102667. http://dx.doi.org/10.1016/j.apor.2021.102667.

Ringwood, J.V., 2025. Control co-design for wave energy systems. Appl. Ocean Res. 158, 104514. http://dx.doi.org/10.1016/j.apor.2025.104514.

Robertson, B., Bailey, H., Clancy, D., Ortiz, J., Buckham, B., 2016. Influence of wave resource assessment methodology on wave energy production estimates. Renew. Energy 86, 1145–1160. http://dx.doi.org/10.1016/j.renene.2015.09.020.

Rusch, C., Crisp, C., Hammagren, E., Prudell, J., Thomson, J., 2023. Wave energy converter power take-off characterization: comparing dynamometer and field data. In: Proceedings of the European Wave and Tidal Energy Conference. vol. 15, http://dx.doi.org/10.36688/ewtec-2023-293.

Rusch, C.J., Hartman, A.R., Maurer, B.D., Polagye, B.L., 2021. Influence of heave plate topology on reaction force. Ocean Eng. 241, 110054. http://dx.doi.org/10.1016/j.oceaneng.2021.110054.

Rusch, C., Joslin, J., Maurerinst, B., Polagye, B., 2022. Effect of heave plate hydrodynamic force parameterization on a two-body wave energy converter. J. Ocean. Eng. Mar. Energy 8, 355–367. http://dx.doi.org/10.1007/s40722-022-00236-z.

Rusch, C.J., Mundon, T.R., Maurer, B.D., Polagye, B.L., 2020. Hydrodynamics of an asymmetric heave plate for a point absorber wave energy converter. Ocean Eng. 215, 107915. http://dx.doi.org/10.1016/j.oceaneng.2020.107915.

Rusch, Curtis, Thomson, Jim, Crisp, Corey, (2025), TigerRAY drifting tests and wave data – Lake Washington and Puget Sound, February 2023. Marine and Hydrokinetic Data Repository (MHKDR). URL: https://mhkdr.openei.org/submissions/625.

Ruzzo, C., Muggiasca, S., Malara, G., Taruffi, F., Belloli, M., Collu, M., Li, L., Brizzi, G., Arena, F., 2021. Scaling strategies for multi-purpose floating structures physical modeling: state of art and new perspectives. Appl. Ocean Res. 108, 102487. http://dx.doi.org/10.1016/j.apor.2020.102487.

Sheng, W., 2025. An experimental study for improving performance of a cylindrical owc wec with a heave plate. Renew. Sustain. Energy Rev. 214, 115517. http://dx.doi.org/10.1016/j.rser.2025.115517.

Sheng, W., Alcorn, R., Lewis, T., 2014. Physical modelling of wave energy converters. Ocean Eng. 84, 29–36. http://dx.doi.org/10.1016/j.oceaneng.2014.03.019.

So, R., Michelen, C., Bosma, B., Lenee-Bluhm, P., Brekken, T.K.A., 2017. Statistical analysis of a 1:7 scale field test wave energy converter using wec-sim. IEEE Trans. Sustain. Energy 8, 1118–1126. http://dx.doi.org/10.1109/TSTE.2017.2656863.

Sugiura, K., Sawada, R., Nemoto, Y., Haraguchi, R., Asai, T., 2020. Wave flume testing of an oscillating-body wave energy converter with a tuned inerter. Appl. Ocean Res. 98, 102127. http://dx.doi.org/10.1016/j.apor.2020.102127.

Thomson, J., 2012. Wave breaking dissipation observed with swift drifters. J. Atmos. Ocean. Technol. 29, 1866–1882. http://dx.doi.org/10.1175/JTECH-D-12-00018.1.

WAMIT, (2015), Version 7.2 User Manual, Massachusetts Institute of Technology, Cambridge, MA, USA, URL: https://www.wamit.com/manualupdate/v72_manual.pdf.

Wilson, D.G., Bacelli, G., Coe, R.G., Bull, D.L., Abdelkhalik, O., Korde, U.A., Robinett, R.D., 2016. A Comparison of WEC Control Strategies. Technical Report, Sandia National Laboratories, http://dx.doi.org/10.2172/1431291.

Windt, C., Davidson, J., Ringwood, J.V., 2021. Numerical analysis of the hydrodynamic scaling effects for the wavestar wave energy converter. J. Fluids Struct. 105, 103328. http://dx.doi.org/10.1016/j.jfluidstructs.2021.103328.

Wu, J., Qian, C., Ni, Z., Zheng, S., 2021. Impact of the buoy geometry on power absorption of a point absorber with a cylindrical buoy under motion constraint. Appl. Ocean Res. 111, 102680. http://dx.doi.org/10.1016/j.apor.2021.102680.

Xu, Q., Li, Y., Yu, Y.H., Ding, B., Jiang, Z., Lin, Z., Cazzolato, B., 2019. Experimental and numerical investigations of a two-body floating-point absorber wave energy converter in regular waves. J. Fluids Struct. 91, 102613. http://dx.doi.org/10.1016/j.jfluidstructs.2019.03.006.

Xu, S., Wang, S., Soares, C.G., 2021. Experimental investigation on the influence of hybrid mooring system configuration and mooring material on the hydrodynamic performance of a point absorber. Ocean Eng. 233, 109178.

Yu, H., Bai, Z., Shi, Y., Zhao, C., Liu, X., Wang, Y., 2024. Hydrodynamic performance of an elastic capsule oscillating water column type wec: An experimental study. Appl. Ocean Res. 142, 103850. http://dx.doi.org/10.1016/j.apor.2023.103850.

Zang, Z., Zhang, Q., Qi, Y., Fu, X., 2018. Hydrodynamic responses and efficiency analyses of a heaving-buoy wave energy converter with pto damping in regular and irregular waves. Renew. Energy 116, 527–542. http://dx.doi.org/10.1016/j.renene.2017.09.057.

Zou, S., Abdelkhalik, O., Robinett, R., Bacelli, G., Wilson, D., 2017. Optimal control of wave energy converters. Renew. Energy 103, 217–225. http://dx.doi.org/10.1016/j.renene.2016.11.036.